J. Fluid Mech. (1987), *vol.* 185, *pp.* 1–30
Printed in Great Britain

Simulation of flow between concentric rotating spheres. Part 1. Steady states

By PHILIP S. MARCUS
Department of Mechanical Engineering, University of California, Berkeley, CA 94720, USA

AND LAURETTE S. TUCKERMAN
Department of Physics, University of Texas, Austin, TX 78712, USA

(Received 22 March 1985 and in revised form 16 March 1987)

Axisymmetric spherical Couette flow between two concentric differentially rotating spheres is computed numerically as an initial-value problem. The time-independent spherical Couette flows with zero, one and two Taylor vortices computed in our simulations are found to be reflection-symmetric about the equator despite the fact that our pseudospectral numerical method did not impose these properties. Our solutions are examined for self-consistency, compared with other numerical calculations, and tested against laboratory experiments. At present, the most precise laboratory measurements are those that measure Taylor-vortex size as a function of Reynolds number, and our agreement with these results is within a few per cent. We analyse our flows by plotting their meridional circulations, azimuthal angular velocities, and energy spectra. At Reynolds numbers just less than the critical value for the onset of Taylor vortices, we find that pinches develop in the flow in which the meridional velocity redistributes the angular momentum. Taylor vortices are easily differentiated from pinches because the fluid in a Taylor vortex is isolated from the rest of the fluid by a streamline that extends from the inner to the outer sphere, whereas the fluid in a pinch mixes with the rest of the flow.

1. Introduction

1.1. *Motivation*

In this paper we examine numerically the steady-state, axisymmetric incompressible flow between two concentrically rotating spheres. In many ways, this 'spherical Couette' flow resembles the Taylor–Couette flow between differentially rotating cylinders, especially in the equatorial regions of the sphere where the centrifugal force on the flow is greatest. For example, spherical Couette flow, like Taylor–Couette flow has a critical Reynolds number, Re_c, such that for $Re \geqslant Re_c$ Taylor vortices are formed. However, the number of vortices depends on the gap width between the inner and outer spheres, though the vortices are always confined to the equatorial region. (For very wide gaps they may not occur at all.) There are other qualitative differences between rotating flows in cylinders and spheres due to the strong Ekman pumping in the latter at the poles. In fact, near the poles spherical Couette flow looks more similar to the flow between two differentially rotating, parallel plates than it does to Taylor–Couette flow. We shall show that spherical Couette flow has a large number of allowable states and an intriguing variety of transitions among them.

Although spherical Couette flow is more relevant than Taylor–Couette flow to

most astrophysical, geophysical, and engineering applications, it has been studied less because it is more difficult to treat analytically and because precision laboratory experiments in rotating spheres (where the inner sphere must be suspended and prevented from wobbling by fine wires) are much more unwieldly than the experiments with rotating cylinders. Yet, spherical Couette flow is no more difficult to simulate numerically than is Taylor–Couette flow in an 'infinitely long cylinder (i.e. in a flow where axial periodicity is imposed arbitrarily). In fact, it is easier to simulate spherical Couette flow than to simulate Taylor–Couette flow in finite-length cylinders due to the discontinuity in the boundary conditions of the latter flow at the axial end plates. Taylor–Couette flow in finite cylinders has become of increasing interest recently because it has been shown that the bifurcation/stability diagrams and pattern selection (or axial wavelength selection) mechanisms are different in infinite and in finite-length geometries (Benjamin 1978*a*, *b*; Benjamin & Mullin 1981, 1982; Mullin 1982; Cliffe 1983). In many respects, spherical Couette flow, with its finite boundaries in all directions, more closely resembles Taylor–Couette experiments in finite-length cylinders than do the studies of infinite-length Taylor–Couette flows.

In this study of spherical Couette flow, we limit ourselves to the case where the outer sphere is held stationary. For this flow, there are only two control parameters that describe the experiments: a dimensionless gap width between the spheres $\sigma \equiv (R_2 - R_1)/R_1$ and a Reynolds number $Re \equiv (R_1^2 \Omega_1)/\nu$, where R_1 and R_2 are the inner and outer radii, Ω_1 is the angular velocity of the inner sphere, and ν is the kinematic viscosity. Spherical Couette flow has fewer control parameters than cylindrical Taylor–Couette flow which has the additional control parameter of the dimensionless axial length of the cylinders, or with infinitely long cylinders, the imposed axial wavelength.

In this paper we consider axisymmetric steady-state flows, and in Part 2 we consider the time-dependent transitions among the steady-state equilibria. It is the purpose of this paper to describe the physics and mathematics of the steady states. This provides the framework needed to understand the time-dependent transitions described in Part 2.

A brief discussion of the laboratory observations and the previous numerical and analytic calculations of steady-state spherical Couette flows appears in §1. In §2 we review our method of calculation, highlighting its novel techniques, and in §3 we give evidence that it is an accurate numerical procedure by performing self-consistency tests and by comparing our calculations with other numerical computations and with laboratory experiments. The body of the paper focuses on the detailed descriptions of our simulations of three axisymmetric steady states which are characterized respectively by zero, one and two Taylor vortices on either side of the equatorial plane, which we shall refer to as the 0-, 1- and 2-Taylor-vortex flows. Presentations of the two-dimensional projections of the velocity, bifurcation diagrams, torque calculations, energy spectra, and an analysis of the physically important features of these three flows are presented. Our conclusions are in §5.

1.2. *Review of previous laboratory results*

In this section we review the previous experimental studies of steady-state spherical Couette flow in 'medium-gap' geometries, i.e. those with $0.12 < \sigma < 0.24$. A thorough review of wide- and narrow-gap flows is given by Tuckerman (1983). We define the upper bound of the medium-gap regime at $\sigma = 0.24$ due to the laboratory observation of Belyaev, Monokhov & Yavorskaya (1978) that Taylor vortices never

form in flows with $\sigma > 0.24$. Our definition of the lower bound of the medium-gap regime is predicated on Khlebutin's (1968) empirical finding that the torque–Reynolds number relationship of Taylor-vortex flows changes at $\sigma = 0.12$. In medium gaps, Khlebutin was the first to discover the existence of a critical Reynolds number, Re_c, below which he could not visually detect Taylor vortices and above which he found vortices symmetrically arranged on both sides of the equator.

Sawatzki & Zierep (1970), Zierep & Sawatzki (1970) and Wimmer (1976), examined the medium-gap regime in more detail by studying flows in several geometries including one with $\sigma = 0.18$. They found that below Re_c, the non-dimensional torque τ exerted on the outer stationary sphere by the flow (with no Taylor vortices) is proportional to Re^{-1}. (Here, and throughout the remainder of the paper, we non-dimensionalize by choosing the unit of length as R_1, time as Ω_1^{-1} and mass as ρR_1^3, where ρ is the fluid density.) By contrast, for flows with Taylor vortices, they found that $\tau \propto Re^{-\frac{1}{2}}$ in good agreement with Khlebutin and also with the experiments of Munson & Menguturk (1975).

Although Wimmer observed non-axisymmetric and time-dependent flows for $\sigma = 0.18$, he did not find any axisymmetric equilibria that were not reflection-symmetric about the equator. Sawatzki & Zierep, along with Wimmer found that the spherical Couette flows are non-unique; that is, the state of the flow not only depends on Re and σ, but also on the past history of the flow. In particular, the final state is a function of the acceleration rate of the inner sphere to its final value (see Part 2).

1.3. *Analytics and numerics*

We note that very few calculations have been done in the medium-gap regime. This is due to the fact that unlike Taylor–Couette flow in infinite-length cylinders, the flow between two rotating spheres has no closed-form (subcritical), 0-vortex solution about which to perform linear perturbation theory. Approximate 0-vortex solutions calculated with finite sums of Legendre polynomials converge fastest (Walton 1978) at small values of σ (narrow-gap). The wide-gap regime can be studied in the limit $R_2 \to \infty$, which corresponds to a sphere rotating in an unbounded fluid (Howarth 1954). Most analytic or quasi-analytic calculations are therefore in the narrow- and wide-gap regimes (Munson & Joseph 1971*a*, *b*; Soward & Jones 1983).

Because of the wealth of laboratory data available from the experiments of Wimmer, we restrict the numerical study in this paper to $\sigma = 0.18$. For the same reason, the flows with $\sigma \approx 0.18$ have been studies as initial-value problems by Bonnet & Alziary de Roquefort (1976), Bartels (1982) and Dennis & Quartapelle (1984), and as a steady (not necessarily stable) solution of the time-independent equations by Schrauf (1983*a*). Frequent comparisons between these numerical studies and ours will be made throughout this paper, but because these earlier papers were primarily concerned with stability or transitions we defer a more thorough discussion of them to Part 2.

2. Method of solution

2.1. *Basic equations and Stokes solution*

The velocity, $\boldsymbol{u}$, of a constant-density fluid between two concentric spheres at R_1 and R_2 where the outer one at R_2 is held fixed and the inner is rotated at angular velocity Ω_1 is determined by the Navier–Stokes equation:

$$\frac{\partial \boldsymbol{u}}{\partial t} + (\boldsymbol{u} \cdot \nabla)\, \boldsymbol{u} = -\nabla P + \frac{1}{Re} \nabla^2 \boldsymbol{u}, \tag{2.1}$$

the equation of incompressibility:

$$\nabla \cdot \boldsymbol{u} = 0, \tag{2.2}$$

and the no-slip boundary conditions at the inner rotating and outer fixed radii:

$$\boldsymbol{u}(r = 1, \theta, \phi) = \sin\theta\, \hat{\boldsymbol{e}}_\phi, \quad \boldsymbol{u}(r = 1+\sigma, \theta, \phi) = 0. \tag{2.3}$$

We have non-dimensionalized equations (2.1)–(2.3) by the choice of units given in §1.

We shall refer to the ϕ-component of the velocity u_ϕ as the azimuthal flow and to the remaining components of the velocity as the meridional flow $\boldsymbol{u}_{\mathrm{m}}$. The Stokes flow $\boldsymbol{u}^*$ is the time-independent solution to (2.1)–(2.3) in the limit $Re \to 0$:

$$\boldsymbol{u}^* = \left(\alpha r + \frac{\beta}{r^2}\right) \sin\theta\, \hat{\boldsymbol{e}}_\phi, \tag{2.4}$$

where α and β depend on σ. Although the Stokes solution is exclusively azimuthal, it is a function of θ. Note that the angular velocity $u^*/r\sin\theta$ is not a function of θ so that each radial shell moves with a constant velocity.

Due to a fortuitous cancellation of the pressure gradient with the nonlinear terms, the Stokes solution to the equations of motion in cylindrical geometries (with infinite aspect ratio) happens also to be a solution to the full nonlinear equations (i.e. circular Couette flow). It should not be surprising that fortuitous cancellations do not also occur in spherical geometries. In spherical Couette flow a small meridional velocity is generated from the nonlinear interaction of the Stokes solution with itself via the advective terms in the Navier–Stokes equation. This causes the true flow to deviate from the Stokes solution at all finite Reynolds numbers. At very small Re, the flow is still mostly azimuthal and does not depart greatly from Stokes flow. The meridional motion which is driven by Ekman pumping, expels fluids out from the poles along the surface of the rotating inner sphere. The streamlines resulting from the superposition of the azimuthal and the weaker meridional motion are helices. Despite being three-dimensional, the flow remains axisymmetric (i.e. axisymmetric with swirl).

2.2. *Stream function formalism*

With the assumption of axisymmetry, (2.2) and the three components of (2.1) reduce to two scalar equations. Using the stream function–vorticity formulation, we define a scalar function $\psi(r, \theta, t)$ such that the meridional flow is

$$\boldsymbol{u}_{\mathrm{m}} = \nabla \times (\psi \hat{\boldsymbol{e}}_\phi), \tag{2.5}$$

or equivalently,

$$u_r = \frac{1}{r\sin\theta} \frac{\partial \psi \sin\theta}{\partial \theta}, \tag{2.6}$$

$$u_\theta = -\frac{1}{r} \frac{\partial r\psi}{\partial r}. \tag{2.7}$$

We also define a scalar function $\omega(r, \theta, r)$ by

$$u_\phi \hat{\boldsymbol{e}}_\phi = \boldsymbol{u}^* + \omega \hat{\boldsymbol{e}}_\phi, \tag{2.8}$$

where $\boldsymbol{u}^*$ is the Stokes flow defined in (2.4). The two scalar equations that we seek will contain a Laplacian-like operator, A^2, which we define by

$$\mathrm{A}^2 f \equiv \left(\nabla^2 - \frac{1}{r^2 \sin^2\theta}\right) f = \hat{\boldsymbol{e}}_\phi \cdot \nabla^2 (f \hat{\boldsymbol{e}}_\phi). \tag{2.9}$$

Note that the axisymmetry of ψ implies that the ϕ component of the vorticity is

$$\hat{\boldsymbol{e}}_\phi \cdot \nabla \times [\nabla \times \psi \hat{\boldsymbol{e}}_\phi] = -\mathrm{A}^2 \psi. \tag{2.10}$$

In terms of A^2, ω, and ψ, we have the following equations for the ϕ equations of the velocity and of the vorticity:

$$\frac{\partial \omega}{\partial t} = \hat{\boldsymbol{e}}_\phi \cdot \boldsymbol{u} \times (\nabla \times \boldsymbol{u}) + \frac{1}{Re} \mathrm{A}^2 \omega, \tag{2.11}$$

$$\frac{\partial \mathrm{A}^2 \psi}{\partial t} = -\hat{\boldsymbol{e}}_\phi \cdot \nabla \times [\boldsymbol{u} \times \nabla \times \boldsymbol{u}] + \frac{1}{Re} \mathrm{A}^4 \psi. \tag{2.12}$$

No-slip boundary conditions (2.3) along the spherical boundaries and the assumption of axisymmetry imply the following boundary conditions for ω and ψ:

$$\omega, \psi = 0 \quad \text{at } \theta = 0, \quad \theta = \pi, \tag{2.13}$$

$$\omega, \psi = 0 \quad \text{at } r = 1, \quad r = 1 + \sigma, \tag{2.14}$$

$$\frac{\partial \psi}{\partial r} = 0 \quad \text{at } r = 1, \quad r = 1 + \sigma. \tag{2.15}$$

2.3. *Numerical representation*

We use the pseudospectral or collocation method in our calculations; functions are represented both in spectral space, as a finite series of basis functions and in physical space at grid points (Lanczos 1956). Derivatives are taken in spectral space, and multiplications are done in physical space; in the appropriate spaces both operations are exact and inexpensive. The transforms between spectral and physical space are numerically cheap (but not exact due to aliasing and truncation) and are done by fast Fourier transforms. Each term in the spectral sum is a product of a basis function in θ and a basis function in r. In the radial direction, we use Chebyshev polynomials, which are well known for their fast convergence properties and ability to resolve thin boundary layers (Gottlieb & Orszag 1977). In the θ-direction ($0 \leqslant \theta \leqslant \pi$) we use sine functions.

Because each sine term in the expansion satisfies the homogeneous θ boundary conditions (2.13) exactly, the θ-expansion is a Galerkin expansion and no further θ boundary conditions need to be applied. In contrast, the radial Chebyshev polynomials do not satisfy the radial boundary conditions (equations (2.14) and (2.15)) and further constraints must be imposed on the radial expansions (see below).

Note that we are not restricting the θ-expansion in a way such that the fluid velocity must be reflection-symmetric about the equator. That restriction is equivalent to including only the sine terms, $\sin(n\theta)$, with n odd in the $\tilde{\omega}$ expansion, and n even in the ψ expansion.

Previous authors (e.g. Bratukhin 1961; Yakushin 1969; Munson & Joseph 1971*a*, *b*; Astaf'eva, Vvedenskaya & Yavorskaya 1978) have used Legendre polynomials in the θ-direction because they are the natural basis functions for a spherical geometry, in that they are the eigenfunctions of the θ-part of the Laplacian. (The associated Legendre polynomials P_n^1 are the eigenfunctions of the θ-part of the operator A^2 defined above.) We have chosen to expand ω and ψ in Fourier series to take advantage of fast Fourier transforms. Although analogous fast Legendre transforms exist, at present they are not as fast as their Fourier counterparts.

Although A^2 is not diagonal when written with a Fourier series basis, it is upper triangular, and therefore easy to invert (see below).

Although convenient to work with, sine series have the disadvantage of equally spaced collocation points in θ, whereas spherical Couette flow has most of its spatial structure near the equator. Legendre series expansions are not an improvement since their collocation points are also nearly equally spaced in θ. It is probable that the most economical spatial representation of the flow would be to first map θ from the interval $0 \leqslant \theta \leqslant \frac{1}{2}\pi$ to the interval $[0, 1]$ and $\frac{1}{2}\pi \leqslant \theta \leqslant \pi$ to the interval $[-1, 0]$. Then one would expand each of the two intervals as odd Chebyshev series (which are complete in the specified intervals, converge exponentially, and satisfy exactly the boundary conditions (2.13) and match the two series at the equator). With this method, most of the collocation points would be near the equator.

To integrate in time, we use the Adams–Bashforth method with the nonlinear terms and the implicit Crank–Nicholson method with the viscous terms. The temporal finite-difference equations that are produced from (2.11) and (2.12) are:

$$C^2\omega(t+\Delta t) = \omega(t)+\tfrac{1}{2}\Delta t[3J_\omega(t)-J_\omega(t-\Delta t)]+\frac{\Delta t}{2Re}A^2\omega(t), \tag{2.16}$$

$$C^2\xi(t+\Delta t) = \xi(t)+\tfrac{1}{2}\Delta t[3J_\xi(t)-J_\xi(t-\Delta t)]+\frac{\Delta t}{2Re}A^2\xi(t), \tag{2.17}$$

and

$$A^2\psi(t+\Delta t) = \xi(t+\Delta t), \tag{2.18}$$

where

$$C^2 = I-\frac{\Delta t}{2Re}A^2, \tag{2.19}$$

$$J_\omega \equiv \hat{\boldsymbol{e}}_\phi\cdot[\boldsymbol{u}\times(\nabla\times\boldsymbol{u})], \tag{2.20}$$

$$J_\xi \equiv -\hat{\boldsymbol{e}}_\phi\cdot\{\nabla[\boldsymbol{u}\times(\nabla\times\boldsymbol{u})]\}. \tag{2.21}$$

2.4. *Inversion of the elliptic equations*

The only difficulty in the numerical implementation of these equations is the inversion of the operators C^2 and A^2 that appear on the left-hand side of equations (2.16)–(2.18) while imposing the radial boundary conditions. We will show that this can be done using time and storage proportional to the number of sine modes in θ.

We begin by defining the operators A_r^2 and A_θ^2 by

$$A_r^2 \equiv \frac{\partial}{\partial r}r^2\frac{\partial}{\partial r}, \tag{2.22}$$

$$A_\theta^2 \equiv \frac{1}{\sin\theta}\frac{\partial}{\partial\theta}\sin\theta\frac{\partial}{\partial\theta}-\frac{1}{\sin^2\theta}, \tag{2.23}$$

so that

$$r^2A^2 = A_r^2+A_\theta^2. \tag{2.24}$$

Note that r^2A^2 is separable in r and θ, whereas A^2 is not. Therefore it is easier to solve an elliptic equation of the form

$$r^2A^2F(r,\theta) = r^2G(r,\theta). \tag{2.25}$$

When the operator $\boldsymbol{A}_\theta^2$ is represented as a matrix (which acts upon vectors whose

elements are the sine Fourier components), it is upper triangular. The (j,k)th element of $\boldsymbol{A}_\theta^2$ is

$$\boldsymbol{A}_\theta^2(j,k) \equiv \frac{2}{\pi}\int_0^\pi \sin(j\theta)\,\boldsymbol{A}_\theta^2 \sin(k\theta)\,\mathrm{d}\theta. \tag{2.26}$$

The only non-zero elements of $\boldsymbol{A}_\theta^2$ are

$$a_{jk} \equiv \mathrm{A}_\theta^2(j,k) = \begin{cases} -j(j+1) \equiv b_j & \text{for } k=j, \\ -2\mathrm{j} \equiv \tilde{b}_j & \text{for } k>j, \quad (j+k) \text{ even}. \end{cases} \tag{2.27}$$

Due to the Dirichlet boundary conditions that must be imposed at $r=1$ and at $r=1+\sigma$, $\boldsymbol{A}_r^2$ is not an upper triangular matrix when represented in Chebyshev space. For this reason, and because of our continual need to multiply and divide by r^2, we construct the $\boldsymbol{A}_r^2$ matrix in physical r-space by first computing its action on Chebyshev polynomials and then performing the similarity transform that takes the Chebyshev space into physical r-space.

The full operator $r^2\boldsymbol{A}^2$ can be written as a block matrix in (physical-r)–(sine-θ) space:

$$\begin{bmatrix} \boldsymbol{A}_r^2+b_1\boldsymbol{I} & 0 & \tilde{b}_1\boldsymbol{I} & 0 & \cdots \\ 0 & \boldsymbol{A}_r^2+b_2\boldsymbol{I} & 0 & \tilde{b}_2\boldsymbol{I} & \cdots \\ 0 & 0 & \boldsymbol{A}_r^2+b_3\boldsymbol{I} & 0 & \cdots \\ \vdots & \vdots & \vdots & \mathrm{I} & \vdots \end{bmatrix} \tag{2.28}$$

with $N_\theta \times N_\theta$ blocks, where each block is of size $N_r \times N_r$, where N_r is the number of radial collocation points, where N_θ is the number of sine modes in the expansion, where $\boldsymbol{I}$ is the identity matrix, and where b_k and $\tilde{b}_k$ are defined by (2.27). The vector $\boldsymbol{F}(r,\theta)$ on which this matrix operates is made up of the N_θ vectors $\boldsymbol{f}_k(r)$, with $k=1,\ldots,N_\theta$ and each $\boldsymbol{f}_k$ has length N_r. Similarly, $r^2\boldsymbol{G}(r,\theta)$ is composed of vectors $\boldsymbol{g}_k(r)$.

Because $r^2\boldsymbol{A}^2$ is block upper triangular, (2.25) can be solved for $\boldsymbol{F}(r,\theta)$ by a submatrix back-solve. Using the representation of (2.28), the equation can be reduced to N_θ equations for the $\boldsymbol{f}_k$ where each equation is an $N_r \times N_r$ matrix equation. The equation for $\boldsymbol{f}_{N_\theta}$ is

$$(\boldsymbol{A}_r^2+b_{N_\theta}\boldsymbol{I})\boldsymbol{f}_{N_\theta} = \boldsymbol{g}_{N_\theta}, \tag{2.29}$$

the equation for $\boldsymbol{f}_{N_\theta-1}$ is

$$(\boldsymbol{A}_r^2+b_{N_\theta-1}\boldsymbol{I})\boldsymbol{f}_{N_\theta-1} = \boldsymbol{g}_{N_\theta-1}, \tag{2.30}$$

the equation for f_j, $j \leqslant N_\theta-2$ is

$$(\boldsymbol{A}_r^2+b_j\boldsymbol{I})f_j+\tilde{b}_j \sum_{\substack{k=j+2 \\ k+j=\text{even}}}^{N_\theta} \boldsymbol{f}_k = \boldsymbol{g}_j. \tag{2.31}$$

Because the values of $\tilde{b}_j$ are independent of k, the sum in (2.31) need not be evaluated afresh for each value of j. The submatrix back-solve therefore requires only $O(N_\theta)$ operations per radial collocation point rather than the usual $O(N_\theta^2)$ needed for an arbitrary upper triangular matrix.

To solve (2.29)–(2.31) with homogeneous Dirichlet radial boundary conditions requires a trivial replacement of the top and bottom rows in each of the N_θ matrix equations. The operators, $(\boldsymbol{A}_r^2+b_k\boldsymbol{I})$ (with appropriate replacements for the top and bottom rows) that must be inverted for each of the N_θ equations are identical up to the addition of a constant times $\boldsymbol{I}$. We therefore solve for $\boldsymbol{f}_k$ by inverting each of the

$(N_r \times N_r)$ operators with the eigenvector method (Haidvogel & Zang 1979). The total work needed to solve for all of the $\boldsymbol{f}_k$ is $O(N_\theta N_r^2)$ and the total storage needed to implement the Zang–Haidvogel factorization is $O(N_r^2 + N_\theta)$.

An upper-triangular matrix is stable with respect to back-solving if it is diagonally dominant. The analogous requirement for our block upper-triangular matrix is that $|\lambda + a_{kk}|$ must be greater than $|a_{kj}|$ for all eigenvalues λ of $\boldsymbol{A}_r^2$ and for all $j \neq k$. Our matrices in (2.28) satisfy this stability criterion.

The C^2 operator that appears in (2.16)–(2.17) is inverted in a manner analogous to the one used to invert A^2.

2.5. *Boundary conditions*

When $\omega(t+\Delta t)$ and $\psi(t+\Delta t)$ are determined from (2.16)–(2.18) by inverting the C^2 and A^2 matrices (with the appropriate row substitutions) we are guaranteed that ψ and ω obey homogeneous Dirichlet boundary conditions in r. However, the Neumann radial boundary condition on ψ (equation (2.15)) is, in general, not satisfied. The easiest and computationally least expensive method of inverting C^2 with the correct Neumann boundary conditions on ψ is to use a Green function method, discussed in detail by Marcus (1984*a*). A particular solution, $\xi_p(t+\Delta t)$ and $\psi_p(t+\Delta t)$ is found at each timestep by inverting the C^2 operator with arbitrary (in practice, with homogeneous Dirichlet) boundary conditions, and then inverting the A^2 operator in equation (2.18) with the usual homogeneous Dirichlet boundary conditions. The homogenous solution $\psi_h(t+\Delta t)$ is found easily at each timestep:

$$\psi_h(t+\Delta t) = \sum_{i=1}^{2} \sum_{j=1}^{N_\theta} d_{ij}(t+\Delta t)\, h_{ij}(r,\theta), \tag{2.32}$$

where $d_{ij}(t+\Delta t)$ is a scalar equal to the jth sine Fourier component of $\partial\psi_p/\partial r$ at $r = r_i \equiv 1+(i-1)\sigma$ for $i = 1, 2$. The h_{ij} are a set of linearly independent Green functions and are evaluated only once in a pre-processing step to satisfy

$$C^2 A^2 h_{ij}(r,\theta) = 0, \tag{2.33}$$

$$h_{ij}(r,\theta) = 0 \quad \text{at } r = r_1, r_2, \tag{2.34}$$

$$\frac{\partial h_{ij}}{\partial r}(r,\theta) = \begin{cases} -\sin j\theta & \text{at } r = r_i, \\ 0 & \text{at } r = r_{3-i}. \end{cases} \tag{2.35}$$

Evaluation of the homogeneous solution is inexpensive (since it requires calculating only two radial derivatives of ψ_p for each sine Fourier mode or $O(2N_r N_\theta)$ operations and the accumulation of the sum in (2.32) which requires $O(N_r N_\theta^2)$ operations). The $2N_\theta$ Green functions are quite sparse so that the total storage needed for the set of Green functions is $\frac{1}{2}N_\theta^2 N_r$ (real) words. This is by far the largest block of storage used in solving our initial-value problem. We typically set $N_\theta = 128$ and $N_r = 16$. Although we have not encountered storage problems, we note that it is possible to reduce the storage at the expense, as usual, of an increase in computational time. Rather than store the Green functions we can re-evaluate them at every timestep. This procedure requires two additional block matrix back-solves per timestep and increases the overall computer time by approximately 20%.

2.6. *Eigenmodes and eigenvalues*

An original use we have made of our code is to use it to calculate the eigenmodes and eigenvalues of an equilibrium solution. Surprisingly, this task is readily accomplished

with only a slight modification of our initial-value code. We write the linearized Navier–Stokes equations, governing the evolution of a perturbation $\boldsymbol{u}$ to a given equilibrium $\boldsymbol{U}$ as

$$\left.\begin{aligned} \frac{\partial \boldsymbol{u}}{\partial t} &= Q(\boldsymbol{U})\,\boldsymbol{u}, \\ (Q(\boldsymbol{U}))\,(\boldsymbol{u}) \equiv -(\boldsymbol{u}\cdot\boldsymbol{\nabla})\,\boldsymbol{U} - (\boldsymbol{U}\cdot\boldsymbol{\nabla})\,\boldsymbol{u} - \boldsymbol{\nabla}P + \frac{1}{Re}\,\nabla^2\boldsymbol{u}, \\ \boldsymbol{\nabla}\cdot\boldsymbol{u} &= 0, \end{aligned}\right\} \tag{2.36}$$

The initial-value equation, (2.36), is then solved in the same manner as we solved the fully nonlinear initial-value equations, (2.16)–(2.18), except that the operators J_ω and J_ξ are replaced with J'_ω and J'_ξ

$$\mathrm{J}'_\omega \equiv \hat{\boldsymbol{e}}_\phi\cdot[(\boldsymbol{U}\times(\boldsymbol{\nabla}\times\boldsymbol{u}))+(\boldsymbol{u}\times(\boldsymbol{\nabla}\times\boldsymbol{U}))], \tag{2.37}$$

$$\mathrm{J}'_\xi \equiv -\hat{\boldsymbol{e}}_\phi\cdot[\boldsymbol{\nabla}\times(\boldsymbol{U}\times(\boldsymbol{\nabla}\times\boldsymbol{u}))+\boldsymbol{\nabla}\times(\boldsymbol{u}\times(\boldsymbol{\nabla}\times\boldsymbol{U}))]. \tag{2.38}$$

By evolving equation (2.36) forward in time, $\boldsymbol{u}$ converges to the most unstable eigenmode of $Q(\boldsymbol{U})$. To prevent $\boldsymbol{u}$ from growing too large or too small, we normalize $\boldsymbol{u}$ after each timestep, using the inner product

$$\langle u_1\cdot u_2\rangle \equiv \sum_{n,m} \omega_1(n,m)\,\omega_2(n,m)+\psi_1(n,m)\;\psi_2(n,m), \tag{2.39}$$

where $\omega(n,m)$ and $\psi(n,m)$ are the nth radial Chebyshev and mth azimuthal sine components of the $\omega(r,\theta,t)$ and $\psi(r,\theta,t)$ corresponding to $\boldsymbol{u}(r,\theta,t)$.

Note that by finding the eigenvectors of $Q(\boldsymbol{U})$ with the power method (Dahlquist, Bjorck & Anderson, 1974, chapter 5) we would converge to the eigenvector of $Q(\boldsymbol{U})$ with the largest absolute eigenvalue. Generally this eigenmode is uninteresting because it corresponds to the highly dissipative, high spatial frequency mode whose eigenvalue is approximately equal to $(-1/Re)\,(N_r^2+N_\theta^2)$. The initial-value equation (2.36) is equivalent to the power method for determining the eigenmode $\boldsymbol{u}$ corresponding to the largest absolute eigenvalue of the operator $\exp[Q(\boldsymbol{U})\,\Delta t]$. This eigenmode is, of course, the eigenmode of $Q(\boldsymbol{U})$ with the most positive (or least negative) eigenvalue. The eigenvalue λ of the most unstable mode is determined from (2.36) by calculating the Rayleigh quotient

$$\lambda = \frac{1}{\Delta t}\ln\langle \boldsymbol{u}(t)\cdot\boldsymbol{u}(t+\Delta t)\rangle, \tag{2.40}$$

with the inner product defined by (2.39).

3. Tests of the numerical calculations

We present two types of tests of our calculations. First, we demonstrate that the calculated solutions are self-consistent. Then we show that our computations agree with other numerical calculations and with laboratory experiments.

3.1. *Self-consistency tests*

We can easily test how well our calculated solutions obey angular-momentum and energy-balance equations. We adopt the notation that for any quantity F:

$$\Delta F \equiv F(t'')-F(t'), \quad \int F \equiv \int_{t'}^{t''} F(t)\,\mathrm{d}t.$$

t'	t''	ΔA	$\int \dot{A} - \Delta A$	$\left\lvert\frac{\int \dot{A} - \Delta A}{\Delta A}\right\rvert$	ΔE	$\int \dot{E} - \Delta E$	$\left\lvert\frac{\int \dot{E} - \Delta E}{\Delta E}\right\rvert$
0	4π	-6×10^{-4}	-1×10^{-11}	2×10^{-8}	-4×10^{-2}	-1×10^{-5}	3×10^{-4}
4π	14π	3×10^{-4}	-1×10^{-10}	5×10^{-7}	9×10^{-3}	2×10^{-6}	3×10^{-4}
14π	54π	-3×10^{-5}	-3×10^{-10}	9×10^{-6}	-1×10^{-3}	-5×10^{-7}	4×10^{-4}
54π	160π	-6×10^{-3}	-6×10^{-10}	1×10^{-7}	-1×10^{-1}	4×10^{-6}	3×10^{-5}

TABLE 1. Test of angular momentum and energy balance. During each time interval $[t', t'']$, the exact solution satisfies $\Delta A = \int \dot{A}$ and $\Delta E = \int \dot{E}$. Data is computed from a numerical experiment in which a 0- to 1-vortex transition occurs.

The change in angular momentum, A,

$$A \equiv \int r \sin\theta \, u_\phi \, \mathrm{d}^3x, \tag{3.1}$$

of the fluid is due to the torque exerted on the fluid by the rotating inner sphere τ_1 minus the torque that fluid exerts on the stationary outer sphere, τ_2

$$\Delta A = \int \dot{A} = \int \tau_2 - \tau_1, \tag{3.2}$$

where the torque τ_i is

$$\tau_i = \frac{1}{Re} \int r \sin\theta \left[\frac{\partial u_\phi}{\partial r} - \frac{u_\phi}{r}\right] \mathrm{d}S_i \quad (i = 1, 2), \tag{3.3}$$

and where the surface element $\mathrm{d}S_i$ is evaluated at r_i. (For a steady state, $\tau_2 = \tau_1$ which we denote by τ.) We have calculated the $\tau_i(t)$ at every timestep, and integrated them from time t' to t'' to $O(\Delta t^2)$ accuracy. The quantity $\int [\tau_1 - \tau_2]$ should be equal [to $O(\Delta t)^2$] to ΔA, where ΔA is computed directly by subtracting the angular momenta of our numerically computed solutions at time t'' and t'. We have found numerically that $(\Delta A - \int \dot{A})$ and the error in A itself are both proportional to $(\Delta t)^2$ (as they should be for a code that is second-order accurate in time). In addition, we have found that the fractional error $(\Delta A - \int \dot{A})/\Delta A$ is small. It is a more stringent test of our code if we evaluate the fractional error when the velocity field changes a great deal between time t' and t''. In table 1 we present ΔA, $(\Delta A - \int \dot{A})$, and the fractional error for several pairs of time t' and t'' computed from an initial-value experiment (fully described in Part 2) in which the flow starts as a 0-vortex flow and ends as a 1-vortex flow. The numerical calculations are computed with Δt = inner rotation period/70, $N_\theta = 128$, and $N_r = 32$.

The initial state for the data in table 1 is the equilibrium 0-vortex flow at $Re = 650$. At time $t = 0$ the Reynolds number is set abruptly to $Re = 700$ by lowering the viscosity. From time 0 to 14π there is a systematic undershoot and overshoot of A as a mildly unstable 0-vortex equilibrium is reached. From time 14π to 54π there is hardly any change in the flow field or in A. From time 54π to 160π the change from a 0- to a 1-vortex flow takes place. Since the angular momentum oscillates in time, we have chosen each pair of times, t' and t'', so that A changes monotonically for times between t' and t''. Table 1 shows that the fractional error, $|(\Delta A - \int \dot{A})/\Delta A|$, is less than 10^{-6}.

Using the same initial-value experiment, we have also calculated the numerical errors associated with the energy balance. Energy should be balanced in the sense that

$$\Delta E = \int \dot{E}, \tag{3.4}$$

where $\dot{E} = \dot{E}_{\text{in}} - \dot{E}_{\text{out}}$, where $\dot{E}_{\text{in}}$ is the rate at which energy is pumped into the fluid by the rotating inner cylinder

$$\dot{E}_{\text{in}} = \Omega_1 \tau_1 \quad \text{(in dimensional units)}, \tag{3.5}$$

and where $\dot{E}_{\text{out}}$ is the rate at which energy is viscously dissipated

$$\begin{aligned} \dot{E}_{\text{out}} &= \frac{-1}{Re} \int \boldsymbol{u} \cdot \nabla^2 \boldsymbol{u} \, \mathrm{d}^3 x \\ &= \frac{-1}{Re} \left(\frac{16\pi}{3} + \int (\nabla \times \boldsymbol{u}) \, \mathrm{d}^3 x \right). \end{aligned} \tag{3.6}$$

We have found numerically that the errors in ΔE and $\Delta E - \int \dot{E}$ are proportional to $(\Delta t)^2$. We have also calculated E at each timestep, integrated it (to second order in Δt) from time t' to t'', and then compared it to the value of ΔE computed directly from the difference in energies of the numerically simulated flow at times t' and t''. The results appear in table 1. The fractional error in the energy $|(\Delta E - \int \dot{E})/\Delta E|$, is less than 10^{-4}. While this error is quite small, it is not as small as $|(\Delta A - \int \dot{A})/\Delta A|$. The larger error in the energy is due to the fact that the angular momentum is transferred into, resides in, and is transferred out of the large spatial modes, whereas the energy is produced in the large spatial modes and is dissipated in the small modes. Therefore the balance of energy is a more stringent test of the nonlinear dynamics of the Navier–Stokes equation that couples the large scales to the small scales.

We have determined that our spatial resolution is adequate and that we are free of deleterious truncation and aliasing errors by examining the energy spectrum (see, for example, Marcus (1984*a*) for a discussion of the relationship between spatial resolution and the energy spectrum) and by comparing initial-value, and eigenvalue experiments at different spatial resolutions.

It has been noted that the transition sequence among flows is especially sensitive to the resolution in θ (Bartels 1982). We have found that the transition sequence with $N_\theta = 256$, and $N_r = 32$ is the same as that with $N_\theta = 128$ and $N_r = 16$ for $Re \leqslant 1200$. Eigenvalues calculated with these two different spatial resolutions agree to five significant digits. We therefore conclude that $N_\theta = 128$, $N_r = 16$ is adequate for our studies with $Re \leqslant 1200$. In contrast, calculations with $N_\theta = 64$ and $N_r = 16$ are qualitatively different from the high-resolution calculations (see Part 2).

3.2. *Comparison with other calculations and experiments*

We have used three quantities to compare our results with those of others: (i) the critical Taylor numbers for transitions among the 0-, 1-, and 2-vortex flows, (ii) the torques τ exerted on the outer sphere, and (iii) the sizes of the Taylor vortices.

3.2.1. *Critical Taylor numbers*

Strictly speaking, we should only compare our results at $\sigma = 0.18$ with other numerical calculations and experiments at $\sigma = 0.18$. However, Khlebutin (1968) noted that to a first approximation the critical Taylor number $Ta = Re\,\sigma^{\frac{1}{2}}$ for the onset of Taylor vortices was approximately independent of σ. Therefore, we have included in table 2 a number of numerical and experimental measurements that span a range of σ. We have included four types of transitions: the 0- to 1-vortex transition denoted as $0 \rightarrow 1$ (more frequently called the transition for the onset of Taylor-vortex formation), the reverse transition or $1 \rightarrow 0$, the transition from 0- to 2-vortex flow or $0 \rightarrow 2$, and the reverse transition or $2 \rightarrow 0$. Because transitions may exhibit hysteresis,

	σ	$0 \rightarrow 1$	$1 \rightarrow 0$	$0 \rightarrow 2$	$2 \rightarrow 0$
		Numerical			
This study	0.18	49.8	49.2	56.5	56.5
G. Schrauf (private communication)	0.17647	—	48.4	~ 55.6	~ 55.6
Bartels (1982)	0.17647	—	50.9	55.6–59.3	55.6–59.3
Bonnet & Alziary de Roquefort (1976)	0.17647	—	—	51.9–66.7	51.9–66.7
		Experimental			
Wimmer (1983)	0.18	49.6–49.9	47.7–48.5	61.1–61.9	57.3–57.9
K. Bühler (1983, private communication)	0.154	~ 48.3	~ 48.3	—	~ 54.4
Munson & Menguturk (1975)	0.135	~ 48.1	—	~ 47.8	~ 47.8
Khlebutin (1968)	0.19	44.7 ± 1.6	—	—	—
	Average†	49.0	—	—	—

† Khlebutin's average value of the critical Taylor number determined from 5 different gap sizes.

TABLE 2. Critical Taylor numbers for the transition from a flow with m vortex pairs to a flow with n vortex pairs; ~ indicates that the uncertainties in the measurement were not reported and that the Taylor number was obtained from graphical presentation of the author's data

the critical Taylor number for $m \rightarrow n$ is not necessarily the same as the one for $n \rightarrow m$. In particular, we have found from our calculations that the $0 \rightleftharpoons 1$ transitions have hysteresis but not the $0 \rightleftharpoons 2$ transitions. Some experimental studies (Yavorskaya *et al.* 1977) have specifically stated that hysteresis did not occur in the $0 \rightleftharpoons 1$ transitions. This is not surprising because the measurements of Yavorskaya, Belyaev & Monakhov (1977) were not fine enough to detect the small amount of hysteresis that we observed. We note that when reporting critical Taylor numbers some experimentalists failed to specify whether the observed transition was $0 \rightarrow 1$ or $1 \rightarrow 0$. In these cases we have assumed in table 2 that it is the $0 \rightarrow 1$ transition. Not all numerical studies can measure the critical Taylor number for all types of transitions. For example, a linear stability analysis of the 0-vortex flow will determine the critical Taylor number of the $0 \rightarrow m \neq 0$ transition but not for the $m \rightarrow 0$ transition. Furthermore, previous initial-value codes (Bartels 1982; Astaf'eva *et al.* 1978; Bonnet & Alziary de Roquefort 1976), which sought to measure the critical Ta of the $0 \rightarrow 1$ transition were unable to produce this transition at all.

It should be noted that although there is a wide scatter among both the numerical and the experimental values listed in table 2, the agreements between our numerical calculations and Wimmer's experimental measurements at $\sigma = 0.18$ for the $0 \rightarrow 1$ and $1 \rightarrow 0$ transitions are very good. The agreements between our calculations at $\sigma = 0.18$ and those of Schrauf (1983*a* and personal communication) and Bartels (1982) at $\sigma = 0.17647$ (which, along with ours, are the only high-spatial-resolution calculations listed) are also quite good.

3.2.2. *Torques*

The most common experimental measurement in spherical Couette flow is the torque on the outer sphere τ as a function of Reynolds numbers. We have reported

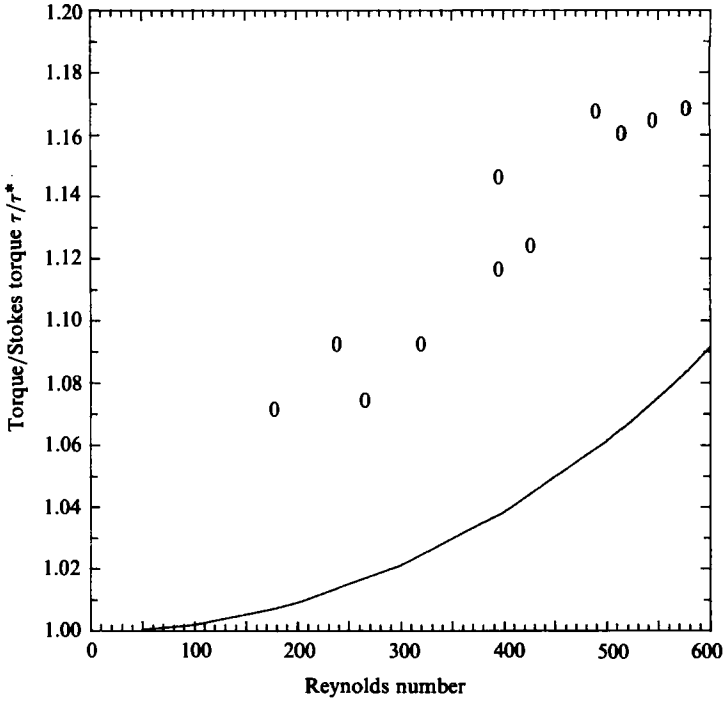

FIGURE 1. Torque/Stokes torque or τ/τ^* for $Re \leqslant Re_c$ from, ——, our numerical simulations, and 0, from laboratory measurements. Note that the experimental points exceed unity by about 7% as $Re \to 0$.

values of torque in units of the torque exerted on the outer sphere by the Stokes flow (equation (2.5)). This Stokes torque, τ^*, in our non-dimensional units is

$$\tau^* = 8\pi \Big/ \left[Re \left(1 - \frac{1}{(1+\sigma)^3} \right) \right]$$

$$= 64.217\, Re^{-1} \quad \text{for } \sigma = 0.18, \tag{3.7}$$

and is, of course, a function of Re.

Wimmer, Khlebutin and Munson & Menguturk have all found experimentally that $\tau \propto Re^{-1}$ for subcritical spherical Couette flow. In figure 1, we plot τ/τ^* for $Re \leqslant 600$ calculated from our numerical simulations (solid curve) and from Wimmer's (private communication, 1983) experimental measurements (denoted by the numeral 0). Wimmer's measurements are consistently about 7% higher than our computed torques, but also 7% higher than that of the Stokes flow for Re as low as 176 (the lowest Reynolds number measured by Wimmer). At such a low Reynolds number (i.e. $Re/Re_c \approx 0.27$), such a large deviation from Stokes flow is not expected. We suggest that Wimmer's torques contain a systematic excess of about 0.07 of the Stokes torque due to the presence of the rods necessary for turning the inner sphere (Zierep, private communication 1983) or due to the intrinsic difficulty in measuring torques to an accuracy of better than a few per cent (Koschmieder, private communication 1983). Although this 7% excess is not important for Wimmer's comprehensive study which ranged over four decades of Re, it is important in our detailed study of the differences between the 0-, 1-, and 2-vortex flows since the torques of the different states usually differ by only a few per cent.

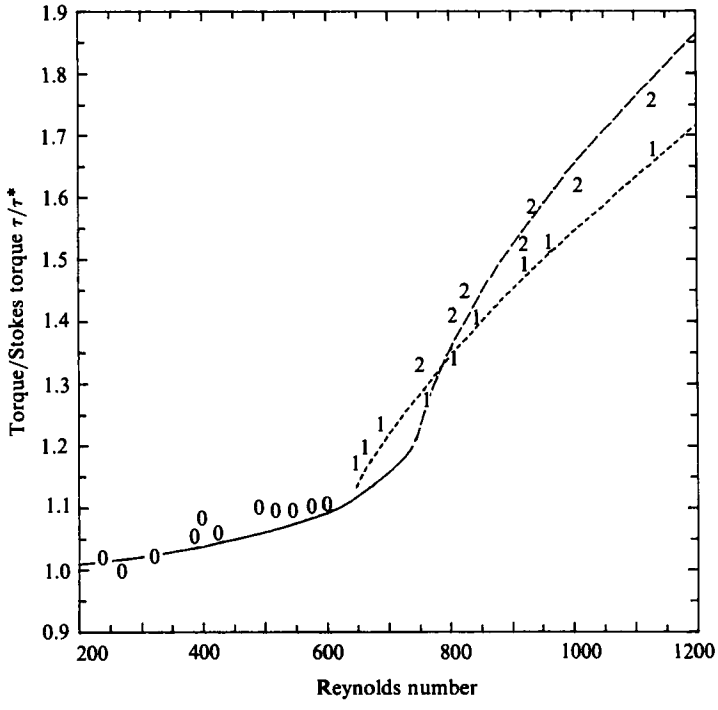

FIGURE 2. τ/τ^* for $200 \leqslant Re \leqslant 1200$ for the numerically computed, ——, 0-, - - - -, 1-, and, – – –, 2-vortex flows. Experimental measurements (with 0.07 subtracted) for each of the three flows are shown respectively by the numerals 0, 1 and 2.

In supercritical spherical-Couette flow, Wimmer found that $\tau \propto Re^{-\frac{1}{4}}$, which is in agreement with the laboratory results of Khlebutin and of Munson & Menguturk. In figure 2 we plot τ/τ^* for $200 \leqslant Re \leqslant 1200$. Wimmer's values (with 0.07 subtracted from each), are represented in the figure by the numerals 0, 1 and 2, which indicate the number of Taylor-vortex pairs in the flow. There is good agreement between Wimmer's corrected experimental and our numerical values of the torques as a function of Re for these three flows.

3.2.3. *Sizes of vortices*

Taylor vortices are approximately circular, so that the ratio of their height to the gap width is near unity. Wimmer found that the exact size of the vortices is strongly dependent on Reynolds number. He measured the size (i.e. distance between the equator and the observed vortex boundary) of the vortex nearest the equator for both the 1- and 2-vortex flows. He found that the non-dimensional sizes varied from 0.54 to 1.3. Unlike the torque, which is a property of the entire flow field (most of which has no Taylor vortices), the vortex size is a very local measurement. In figure 3, we have plotted the sizes of our numerically computed vortices for $600 \leqslant Re \leqslant 1200$ by graphing the distance from the equator to the inflow and outflow boundaries. To facilitate comparison with visual experimental observations (necessarily made from the exterior), these inflow and outflow locations are determined at the radial collocation point nearest to (but not at) the outer sphere. Wimmer's values (1976, private communication, 1983) are indicated as before by the numerals 0, 1 and 2. The short-dashed curve is the size of the vortex of our numerically simulated 1-vortex flows. In the same figure we have also plotted the size of both of the vortices present

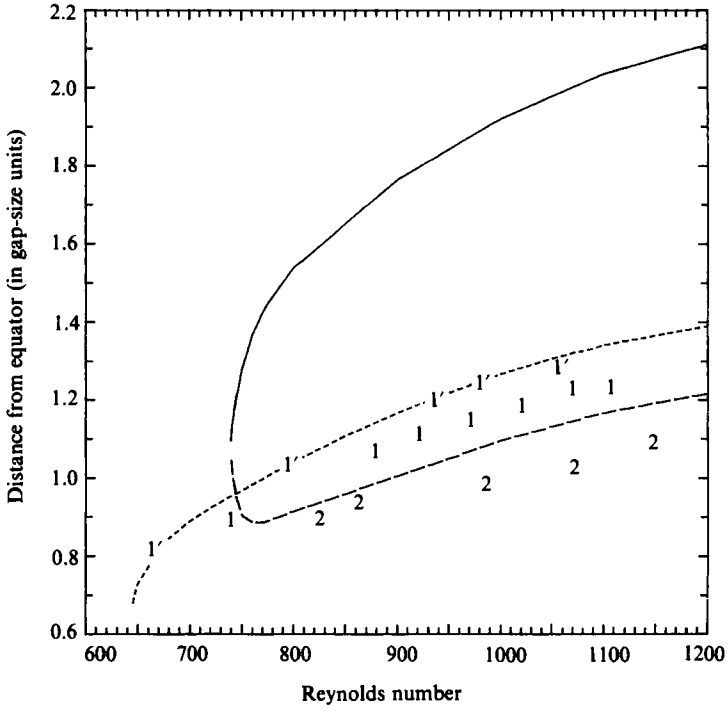

FIGURE 3. ----, size of the vortex in our 1-vortex flows; – – –, size of the vortex closest to the equator in our 2-vortex flows. Size of the vortex farther from the equator in our 2-vortex flows (difference between solid and long-dashed curves). Experimental values of the vortex closer to the equator are shown by numerals that indicate the number of vortex pairs in the flow. The primed numerals represent high precision experiments.

in our 2-vortex flows. Wimmer's measurements of the size of the vortex closer to the equator (denoted by 2) agrees reasonably well with our results (the long-dashed curve). For $Re > 900$ our curves exceed most of Wimmer's data by 5–10%. However, we note that Wimmer performed two separate experiments to measure the size of the vortices in the 1-vortex flow. The experimental values from a very finely controlled experiment are denoted in figure 3 by a numeral 1 with a prime and from an experiment where the angular velocity of the inner sphere is less carefully controlled by an unprimed numeral. Our agreement with the carefully controlled experiment is quite good, whereas the values from Wimmer's two different experiments agree only to within 10%.

We note that in the 2-vortex flow, the sizes of both vortices change abruptly as Re approaches 740 (the lowest Reynolds number for which we have found the 2-vortex state to exist). The solid and long-dashed curves meet at $Re \approx 740$, indicating that the vortex farther from the equator is infinitesimal at onset. Note also that the short-dashed curve indicating vortex size in the 1-vortex state ends at $Re \approx 650$ (the lowest Reynolds number for which we have found the 1-vortex state to exist) with a near-vertical slope. This indicates that the measurement of vortex size as a function of Re is well suited for finding the turning point of a secondary branch in bifurcation diagrams (see Benjamin 1978*b* and Part 2).

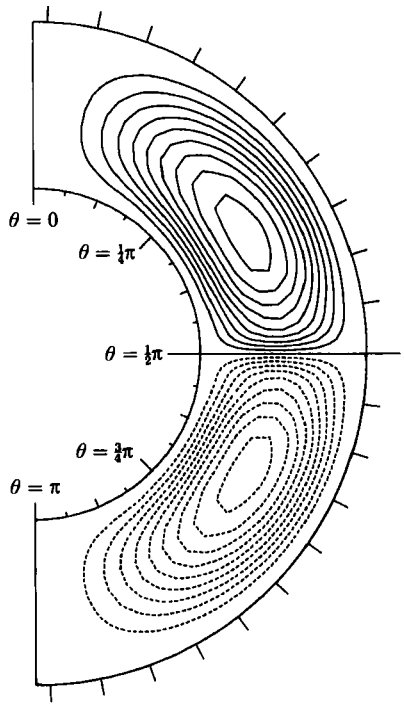

FIGURE 4. (r,θ)-projection of the meridional streamlines of the 0-vortex flow without pinches at $Re = 600$, $\sigma = 0.18$. The two large basic vortices rotate in opposite directions (——, counterclockwise; - - - -, clockwise). The circumferential distance between the tick marks on the outer sphere is σ. The tick marks on the inner sphere are separated by $\frac{1}{16}\pi$ radians. The gap width has been exaggerated by linearly mapping r from the interval $[1, 1+\sigma]$ to $[1, 2]$.

4. Steady-state equilibria

In this section, we present the numerical results and our analysis of the axisymmetric 0-vortex (subcritical) flow and the 1- and 2-vortex (supercritical) flows.

4.1. 0-*Vortex*

Figures 4 and 5 depict the three-dimensional 0-vortex flow at $Re = 600$ and $\sigma = 0.18$. Both figures are two-dimensional projections of the flow on to the (r,θ)-plane at fixed ϕ. In these figures (and all other (r,θ)-projections in this paper) the gap width between the inner and outer spheres is exaggerated for clarity of the features (the radial interval $[1, 1.18]$ is mapped linearly to $[1, 2]$). To provide a guide to this scaling, we have placed tick marks along the outer sphere with a circumferential spacing between tick marks of one gap width. The tick marks along the inner sphere are spaced at intervals of $\frac{1}{16}\pi$ radians; the long pair of tick marks denote the equator. Figure 4 shows the streamlines of the meridional (or (r,θ)-component of the) flow, i.e. contours of constant $r \sin\theta\, \psi(r,\theta)$. The meridional velocity is everywhere tangent to these contours. Streamlines depicting positive (or counterclockwise) circulation are solid contours; those showing negative circulations are dashed. The flow is clearly reflection-symmetric about the equator. The solid (and dashed) streamline located exactly at the equator is the outflow boundary between the two large votices. Note that the spacing between contour lines is only a qualitative guide to the magnitude of the meridional flow since we have used a tanh mapping of the stream function to

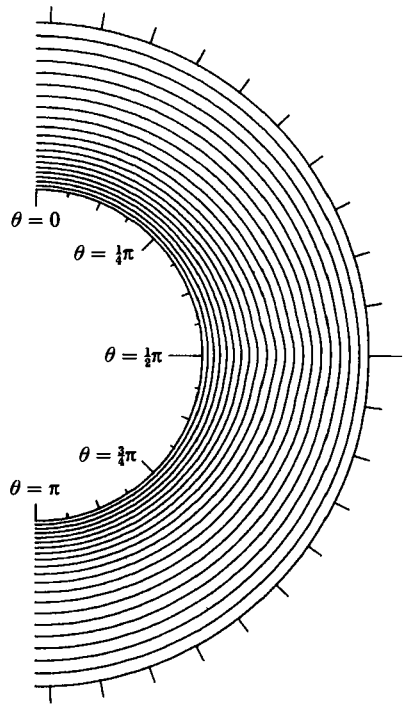

FIGURE 5. Contours of constant angular azimuthal velocity of the 0-vortex flow shown in figure 4. The tick marks and radial stretching are the same as those of figure 4. Except for a slight outward bulge at the equator due to the meridional outflow boundary, the angular velocity is approximately the Stokes flow and independent of θ.

exaggerate weak flow features. The qualitative behaviour of the flow in figure 4 can be understood mathematically by expanding the solution to the Navier–Stokes equation in powers of the Reynolds number. The zeroth-order solution is the Stokes flow, and the first-order correction is a purely meridional velocity of the form

$$u_r = -f(r)\,[3\cos(2\theta)+1] \tag{4.1}$$

and

$$u_\theta = g(r)\sin(2\theta), \tag{4.2}$$

where $f(r)$ and $g(r)$ are functions that can be determined by the power series expansion. The exact forms of f and g need not concern us here but we note that $f(r) \geqslant 0$ for all r while $g(r)$ changes sign at least once in the interval $1 \leqslant r \leqslant 1+\sigma$. The meridional flow in (4.1) and (4.2) is reflection-symmetric about the equator, obtains its maximum radial motion in a radially outward jet at the equator, has radially inward jets at the poles, and looks qualitatively like the flow in figure 4.

The qualitative behaviour of the flow in figure 4 can be understood physically by considering the flow near the poles, where the geometry resembles that between parallel differentially rotating disks. Ekman pumping causes fluid to be thrown outward centrifugally along the rotating disk (inner sphere) and pulled from the centre of the stationary disk (outer sphere). This motion forms the inflow radial boundary jets at the poles. The fluid moving down from the north pole along the inner sphere meets fluid moving up from the south pole at the equator and forms the equatorial radial outflow boundary. The jet divides at the outer sphere and the fluid returns to the two poles along the outer sphere. The fluid in the northern and

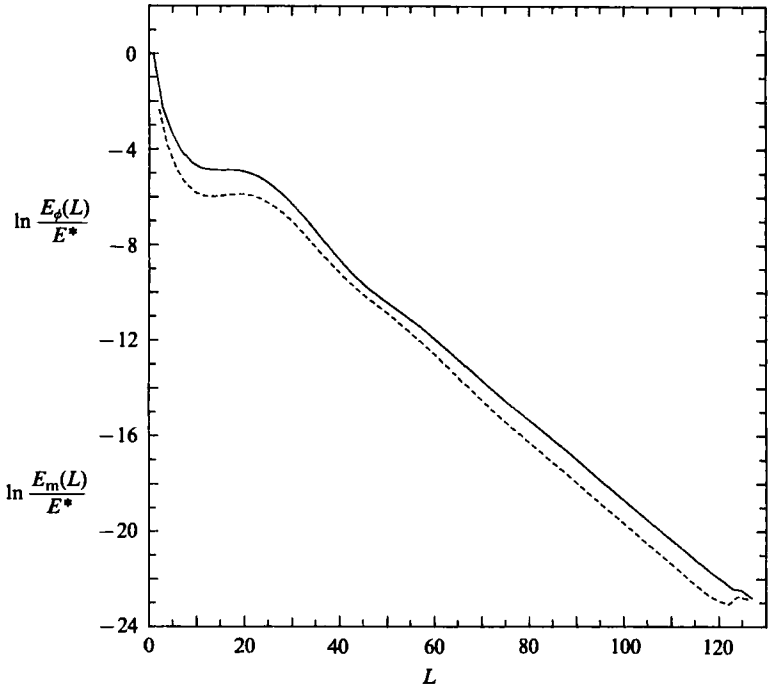

FIGURE 6. ——, the azimuthal $E_\phi(L)$ and, - - - -, meridional $E_m(L)$ spectra of the 0-vortex flow shown in figures 4 and 5. The spectra are discrete; the azimuthal spectrum exists only at the points where L is odd and the meridional spectrum exists only at the points where L is even because the flow is reflection-symmetric about the equator. The flat plateau around $L = 15$ reflects the lengthscale σ.

southern hemispheres do not mix. The inflow and outflow boundaries of the meridional flow are clearly visible in laboratory visualization studies.

Note that in all spherical Couette flows at non-zero Reynolds numbers there is a large-scale meridional circulation present on either side of the equator similar to the flow in figure 4. We shall refer to this large-scale vortical flow as the 'large basic vortex'. This circulation should not be confused with a Taylor vortex. We shall presently describe Taylor vortices; they are qualitatively different from the large basic vortices.

Figure 5 shows the contours of constant angular velocity, $u_\phi/r \sin\theta$, for the flow in figure 4. The angular velocity decreases monotonically from the inner to the outer sphere. For low Re flows, the contours of constant angular velocity are nearly parallel to the spherical boundaries. In fact, they are nearly equal to the angular velocity contours of the Stokes flow (equation (2.5)) which are functions only of radius and not θ. We have stated that in an expansion of the solution of the Navier–Stokes equation in powers of Re, there is no first-order correction to the angular velocity; corrections to the azimuthal velocity come at higher (and even) orders. The effect of these higher-order corrections can be seen in the slight 'wiggles' of the contours near the equator in figure 5. The wiggles are due physically to the redistribution of angular momentum in radius caused by the meridional velocity. We shall show presently how the wiggles increase with increasing Re.

In figure 6 we plot the energy spectra of the flow depicted in figures 4 and 5. To produce figure 6 we decomposed $\boldsymbol{u}$ into vector spherical harmonics $\boldsymbol{Y}_{L,L+1,M}(\theta,\phi)$

which (when multiplied by radial spherical Bessel functions) are eigenfunctions of the vector Laplacian. Using the notation of Edmonds (1960):

$$\boldsymbol{u}(r,\theta,\phi) = \sum_{L=0}^{\infty} \sum_{M=-L}^{L} \sum_{I=-1}^{1} u_{L,L,+I,M}(r)\, \boldsymbol{Y}_{L,L+I,M}(\theta,\phi). \tag{4.3}$$

For an axisymmetric flow field, (4.3) reduces to azimuthal and meridional components

$$u_\phi(r,\theta)\,\hat{\boldsymbol{e}}_\phi = \sum_{L=0}^{\infty} f_L(r)\, \boldsymbol{Y}_{L,L,0}(\theta), \tag{4.4}$$

and

$$\boldsymbol{u}_{\mathrm{m}}(r,\theta) = \sum_{L=0}^{\infty} [g_{L,L+1}(r)\, \boldsymbol{Y}_{L,L+1,0}(\theta) + g_{L,L-1}(r)\, \boldsymbol{Y}_{L,L-1,0}(\theta)]. \tag{4.5}$$

To compute the spectrum the energy is decomposed as follows:

$$E = E_\phi + E_{\mathrm{m}}, \tag{4.6}$$

with

$$E_\phi = \sum_{L=1}^{\infty} E_\phi(L) \equiv \frac{1}{2} \sum_{L=1}^{\infty} \int_1^{1+\sigma} f_L^2 r^2 \,\mathrm{d}r \tag{4.7}$$

and

$$E_{\mathrm{m}} = \sum_{L=1}^{\infty} E_{\mathrm{m}}(L) \equiv \frac{1}{2} \sum_{L=1}^{\infty} \sum_{I=-1,-1} \int_1^{1+\sigma} g_{L,L+I}^2 r^2 \,\mathrm{d}r. \tag{4.8}$$

There is no $L = 0$ component in a divergence-free velocity field with homogeneous normal boundary conditions.

For a flow that is reflection-symmetric (antireflection-symmetric) about the equator, the sums in (4.4) and (4.7) contain only terms with odd (even) L, and the sums in (4.5) and (4.8) contain only even (odd) L, or

$$E(L = \text{odd}) = \left\{ \begin{array}{ll} E_\phi(L) & \text{if reflection-symmetric} \\ E_{\mathrm{m}}(L) & \text{if antireflection-symmetric} \end{array} \right\}, \tag{4.9}$$

$$E(L = \text{even}) = \left\{ \begin{array}{ll} E_{\mathrm{m}}(L) & \text{if reflection-symmetric} \\ E_\phi(L) & \text{if antireflection-symmetric} \end{array} \right\}. \tag{4.10}$$

For a general asymmetric flow, $E(L)$ has contributions from both $E_\phi(L)$ and $E_{\mathrm{m}}(L)$. Since the $E_\phi(L)$ and $E_{\mathrm{m}}(L)$ spectra differ in form and magnitude, we have plotted them separately in figure 6. The solid curve is the azimuthal and the dashed curve the meridional spectrum. The spectra, of course, exist only at discrete points with L = odd for E_ϕ and with L = even for E_{m} since our flow is reflection-symmetric. The continuous curves in figure 6 have been drawn by connecting the 64 ± 1 points of each of the discrete spectra.

The energy in figure 6 is non-dimensionalized by dividing by the energy of the Stokes flow E^*. The salient feature of the spectra is that for large L they decrease exponentially. The flat plateau at $L \approx 15$ corresponds to the lengthscale of the gap width between the inner and outer spheres. (The non-dimensional length associated with any L is approximately π/L.)

4.1.1. 0-*Vortex flow with pinches*

As the Reynolds number is increased, the basic flow develops what Bonnet & Alziary de Roquefort (1976) have called a pinching of streamlines. This pinching is illustrated in figure 7 which is a plot of the meridional streamlines in the (r,θ)-plane (using the conventions of figure 4) of our numerically calculated flow at $Re = 650$,

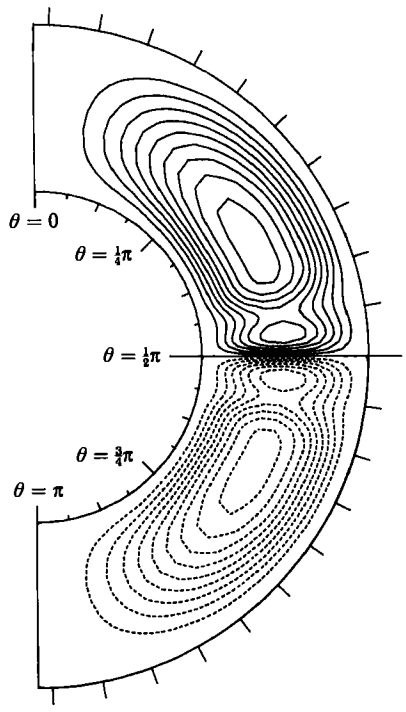

FIGURE 7. The meridional velocity (plotted as in figure 4) of 0-vortex flow with pinches at $Re = 650$ and $\sigma = 0.18$. Although the pinches near the equator have closed streamlines, they are not Taylor vortices.

and $\sigma = 0.18$. The pinch is characterized by a stagnation point (i.e. crossing of streamlines) in the (r, θ)-component of the velocity. Although it is not explicitly shown in figure 7, it is obvious that there must be a crossing of streamlines in each hemisphere somewhere between the closed streamlines of the large basic vortex and the closed streamline of small diameter situated in the pinched part of the flow near the equator. In a pinched 0-vortex flow, there are at least two local maxima in the stream function in each hemisphere.

The pinched 0-vortex flow is reflection-symmetric, the pinch being located about one gap width away from either side of the equator. Figure 7 shows that the closed streamlines in the pinch are not separated from the large basic vortex by a radial inflow or outflow boundary (compare figure 7 with figure 10 below for Taylor vortices). A laboratory observer peering into the fluid through a transparent outer radial boundary would not see the closed streamlines of the pinch since the flow near the radial boundary (i.e. what the observer is most likely to see) differs little from the non-pinched flow. Indeed, from flow visualization alone, an experimentalist would be hard pressed to differentiate between the pinched flow in figure 7 and the non-pinched flow in figure 4. The circulation in the closed streamlines of the 0-vortex pinch always have the same sign as that in the large basic vortex. Although the pinch has a strong radial flow, because it is not separated from the large basic vortex by an inflow or outflow boundary that extends from the inner to the outer sphere, it is not a Taylor vortex. We emphasize this distinction between 0-vortex flow with pinches and flows with Taylor vortices because of confusion in the published literature (cf. the review article by Roesner 1977).

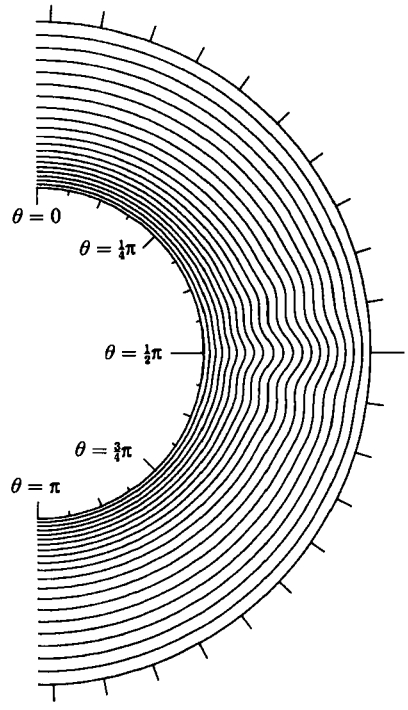

FIGURE 8. The contours of constant azimuthal angular velocity (plotted as in figure 5) for the flow in figure 7. The pinch increases the strength of the meridional outflow at the equator and thereby increases the outward bulge in the contours at the equator.

We have found numerically that pinches occur for $Re \geqslant 630$, and that their development is not accompanied by large abrupt changes in any physical properties of the flow, such as the torque. Figure 8 shows the azimuthal angular velocity contours of the pinched flow in figure 7. The 'wiggles' at the equator have increased in amplitude. The inward and outward bendings of azimuthal contours correspond to meridional flow in the pinch which is radially inward or outward, respectively. The fact that the pinches affect the azimuthal as well as the meridional velocity is also illustrated in the energy spectra in figure 9. In this figure (where we use the conventions of figure 6) we see that both the E_{m} and E_{ϕ} spectra have local maxima at the same place, $L \approx 20$, which is the wavenumber associated with the pinch.

The physical reason for why and where pinches form is related to Taylor-vortex formation. Pinches, like Taylor vortices, have the property of exhibiting a strong correlation between the radial and the azimuthal components of the velocity (Marcus 1984*b*), so both pinches and Taylor vortices are efficient transporters of angular momentum from the rotating inner boundary to the stationary outer boundary. The transport properties of pinches are not only revealed by the equatorial 'wiggles' of the angular velocity contours in figure 8, but also by the angular momentum flux (i.e. the torque) carried by the pinches shown in figure 2. This (τ, Re)-diagram shows a gradual increase in slope at $Re = 630$ (the Reynolds number for the onset of pinches). This increase indicates that the 0-vortex flow with pinches is better at transporting angular momentum than the flow without pinches. Although pinches are not seen in numerical simulations of Taylor-vortex flow in infinitely long cylinders, they have been observed in finite-length cylinders (Keller & Bolstead, private communication 1983). It should not be surprising that in spherical-Couette flow the pinches form first

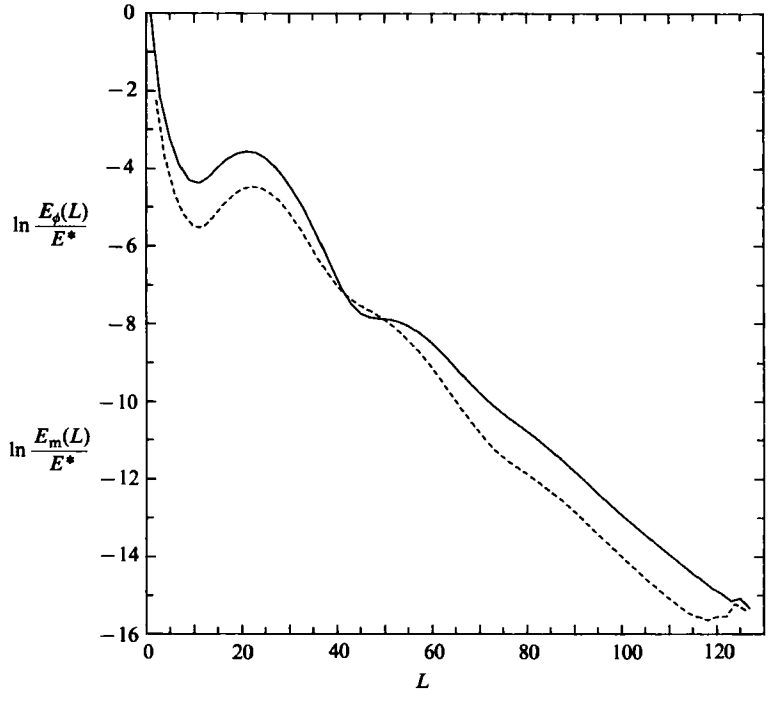

FIGURE 9. $E_\phi(L)$ and $E_m(L)$ spectra (plotted as in figure 6) of the flow in figures 7 and 8. The local maximum at $L \approx 20$ is due to the pinch.

at the equator since it is there that the centrifugal force and angular momentum gradient of the flow are greatest.

4.2. 1-*vortex flow*

An example of the supercritical 1-vortex flow at $Re = 900$ and $\sigma = 0.18$ is shown in the meridional streamlines of figure 10, the contours of constant angular velocity in figure 11 and the energy spectra in figure 12. (All plots use the conventions of figures 4–6.) This axisymmetric and equatorially reflection-symmetric flow corresponds to the Taylor-vortex flow experimentally observed in the laboratory by Sawatzki & Zierep (1970) and Wimmer (1976) and which they labelled 'Mode III'. Figure 11 shows clearly that in each hemisphere there is one Taylor vortex near the equator with a diameter that is approximately equal to a gap width. The Taylor vortex is separated from the large basic vortex by a nearly straight streamline that extends all the way from the inner to the outer radial boundary. This streamline is an outflow boundary and would be clearly visible to a laboratory observer. The circulation in the Taylor and the large basic vortex have the opposite sign. At the equator there is an inflow boundary. Notice that if the pinch of the 0-vortex flow in figure 7 were closed off, the resulting small vortex near the equator would be rotating in the opposite sense of the Taylor vortex in figure 10, and the equator would be an outflow boundary. The transition from a pinched 0-vortex flow with an outflow boundary at the equator to a 1-vortex flow with an inflow boundary at the equator is discussed extensively in Part 2. Stagnation points in the (r, θ)-projection of the velocity in figure 10 occur where the Taylor vortices abut each other and where they abut the large basic vortices. However, these stagnation points are always located on the radial boundaries. In contrast, pinches have their stagnation points located in the

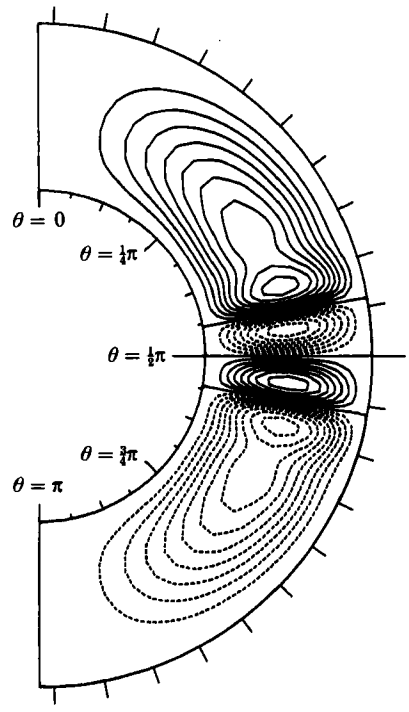

FIGURE 10. Meridional streamlines (plotted as in figure 4) for the $Re = 900$, $\sigma = 0.18$, 1-vortex flow. The Taylor vortices are separated from the large basic vortices by nearly straight radial streamlines (an outflow boundary) that extends from the inner to the outer sphere.

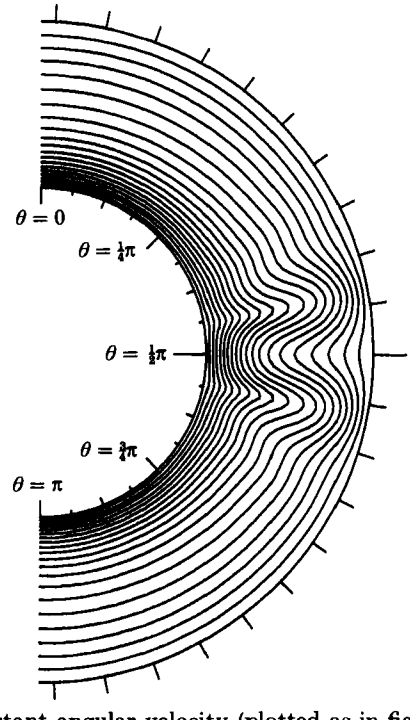

FIGURE 11. Contours of constant angular velocity (plotted as in figure 5) of the flow in figure 10. The inflow boundary at the equator produces an inward bulge there.

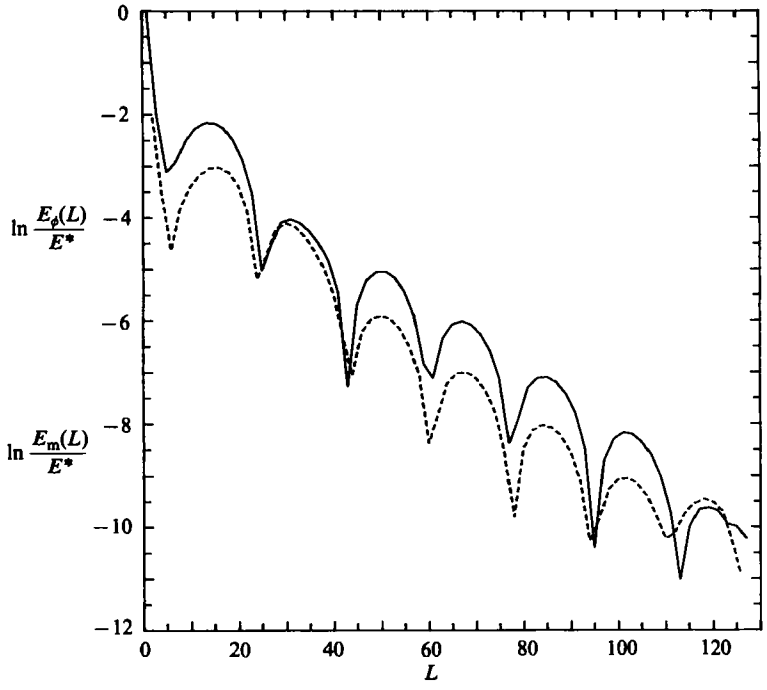

FIGURE 12. $E_\phi(L)$ and $E_m(L)$ (plotted as in figure 6) of the flow in figures 10 and 11. The nearly periodic and exponentially decreasing scallops (rounded local maxima, sharp local minima) are due to a small-scale flow localized at the equator (the Taylor vortices) modulated by a large-scale global flow.

fluid interior (see figure 7). The fact that Taylor vortices are more efficient than pinches at transporting angular momentum is shown in figure 2. For $645 \leqslant Re \leqslant 740$ both the 1-vortex flow and the 0-vortex flow with pinches are equilibria (though not necessarily stable, as will be seen in Part 2). The figure shows that the Taylor vortices in the 1-vortex flow have a greater angular momentum flux than the pinches in the 0-vortex flow.

As the Reynolds number becomes larger, the large basic vortex in the 1-vortex flow develops a pinch. The beginning of this pinch can be seen in figure 10 at approximately 2.5 gap widths away from the equator. Figure 11 shows that the equatorial wiggles in the contours of the azimuthal velocity are more pronounced than those of the pinched 0-vortex flow in figure 8; more importantly, the figure shows that the distortions of the angular velocity contours due to the Taylor vortices are opposite in sign to those due to the pinches – the contours at the equator are pushed radially inward in figure 11 and outward in figure 8.

The spectra of the 1-vortex flow are shown in figure 12. As usual, the azimuthal energy is greater than the meridional energy for almost all L. The most striking feature of figure 12 are the 'scallops' (i.e. the series of rounded local maxima interspersed with sharp local minima) that are spaced almost periodically in L and which decrease exponentially with increasing wavenumber. A scalloped spectrum appears to be a superposition of an infinite number of Gaussians all of the same width and equally spaced but with decreasing amplitude. To see why a scalloped spectrum is reasonable for 1-vortex flow, model the flow's velocity as the product of two parts: the velocity of a Taylor-vortex pair in cylindrical Couette flow (which is axially

periodic with fundamental wavenumber k_0) and an envelope function which confines the Taylor votex to the equator (since spherical Couette flow differs from cylindrical Couette flow in that the former has its vortices confined locally to the equator where the centrifugal force is greatest).

Rather than compute the spectrum of this three-dimensional velocity, we shall compute the energy spectrum, $E(k)$, of a model flow that is characterized by a scalar amplitude $g(\theta)$. Like our axisymmetric velocity fields u_ϕ and u_θ, $g(\theta)$ is to be periodic in θ and vanish at 0 and π (i.e. it is an odd periodic function with a natural representation as a sine series). We simplify further by no longer considering θ to be the polar angle in a spherical geometry, dropping the factor of $\sin\theta$ necessary for volume integration over a sphere to compute $E(k)$

$$E(k) = \left| \frac{1}{2\pi} \int_0^{2\pi} g(\theta)\, \mathrm{e}^{-\mathrm{i}k\theta}\, \mathrm{d}\theta \right|^2, \tag{4.11}$$

where k is a non-negative integer and where $g(\theta)$ is extended antisymmetrically into $\pi < \theta \leqslant 2\pi$. For large wavenumbers, the spectrum defined by (4.11) and the spectrum based on the decomposition of the velocity into spherical harmonics defined by equations (4.4)–(4.8) will look qualitatively similar. We model the envelope function $g_1(\theta)$ as the odd periodic continuation of a Gaussian centred at $\theta = \frac{1}{2}\pi$ with width a.

$$g_1(\theta) \equiv \frac{1}{a} (\tfrac{1}{2}\pi)^{\frac{1}{2}} \sum_{n=-\infty}^{\infty} (-1)^n \exp\left[\frac{-(\theta - \frac{1}{2}\pi - n\pi)^2}{2a^2}\right]. \tag{4.12}$$

The Fourier transform $G_1(k)$ of $g_1(\theta)$ is

$$G_1(k) = \left\{ \begin{array}{ll} \mathrm{i} \exp[-\frac{1}{2}k^2a^2](-1)^{\frac{1}{2}(k-1)} & (k = \text{odd}), \\ 0 & (k = \text{even}). \end{array} \right\} \tag{4.13}$$

The amplitude $g_2(\theta)$ of a Taylor vortex has an exponentially decreasing spectrum (cf. Marcus 1984*b*). We therefore approximate g_2 as

$$g_2(\theta) \equiv \sum_{m=-\infty}^{\infty} \mathrm{e}^{-b|m|k_0}\, \mathrm{e}^{\mathrm{i}mk_0\theta}, \tag{4.14}$$

such that g_2 has period $2\pi/k_0$. The Fourier transform $G_2(k)$ of $g_2(\theta)$ is

$$G_2(k) = \sum_{m=-\infty}^{\infty} \mathrm{e}^{-b|m|k_0}\, \delta_{mk_0,\,k}. \tag{4.15}$$

The energy spectrum $E(k)$ of the amplitude of the total velocity $g(\theta) = g_1(\theta)g_2(\theta)$ is equal to the square of the absolute value of the convolution of G_1 with G_2:

$$E(k) = \left| \frac{1}{2\pi} \int_0^{2\pi} g_1(\theta) g_2(\theta)\, \mathrm{e}^{-\mathrm{i}k\theta} \right|^2 \tag{4.16}$$

$$= \left| \sum_{k'=-\infty}^{\infty} G_1(k-k') G_2(k') \right|^2 \tag{4.17}$$

$$= \sum_n \sum_m \exp\{-\tfrac{1}{2}a^2[(k-nk_0)^2 + (k-mk_0)^2] - bk_0(|n| + |m|)\} (-1)^{k - \frac{1}{2}(m+n)k_0}, \tag{4.18}$$

where k is an integer and where the sum in (4.18) is over all m and n such that $(k-mk_0)$ and $(k-nk_0)$ are odd integers. For $ak_0 > \sqrt{2}$ (i.e. the spacing between

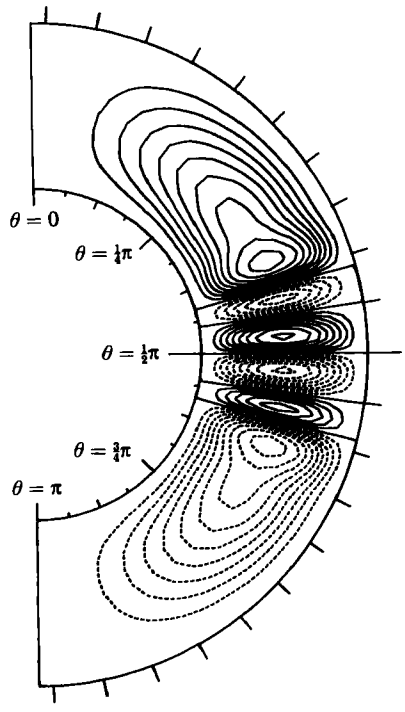

FIGURE 13. Meridional streamlines (plotted as in figure 4) of the 2-vortex flow at the same Re and σ as the 1-vortex flow in figures 10–12.

Gaussians greater than their widths) the only significant terms in the double sum in (4.18) are those with $n = m$, so

$$E(k) \approx \sum_{n=-\infty}^{\infty} \exp\left[-a^2(k-nk_0)^2 - 2bk_0|n|\right], \tag{4.19}$$

where $k-nk_0$ is an odd integer.

The spectrum $E(k)$ in (4.19) has exponentially decreasing rounded maxima located at $k = nk_0$ and sharp minima at

$$k = \tfrac{1}{2}k_0 \pm b/a^2 + nk_0,$$

and looks very much like figure 12. From examining the separation between successive minima (or maxima) in figure 12, we find that $k_0 \approx 17 \approx \pi/\sigma$ and from the width of the Gaussians we see that $a \approx 0.14 \approx 0.8\sigma$. Note that the scale of the spacing between the Gaussians and their widths are both set by σ.

4.3. 2-*Vortex flow*

The (r, θ) meridional velocity of the 2-vortex flow at $Re = 900$ is shown in figure 13. The flow is axisymmetric and reflection-symmetric about the equator and corresponds to the 'Mode IV flow' observed in the laboratory by Sawatzki & Zierep (1970) and Wimmer (private communication 1976). Note that the 2-vortex flow in figure 13 occurs at the same Re and σ as the 1-vortex flow shown in figures 10–12. Both flows are stable equilibria, but figure 2 shows that at $Re = 900$ (and for all $Re > 800$) the 2-vortex has a greater torque than the 1-vortex flow. Therefore, the 2-vortex flow is more efficient at transporting angular momentum for large Re. For

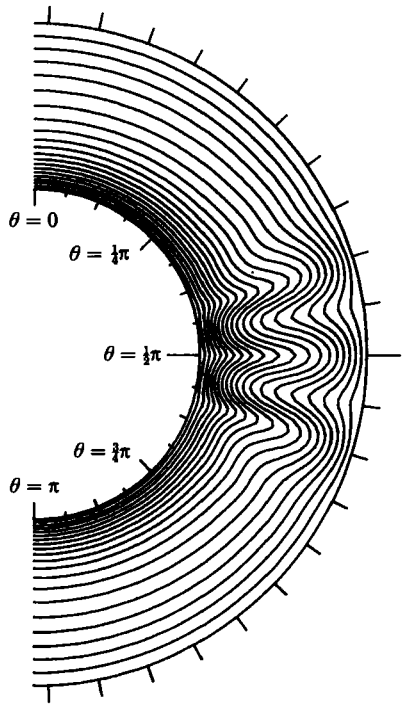

FIGURE 14. Contours of constant angular velocity (plotted as in figure 5) of the flow in figure 13. The outflow boundary at the equator and between the fundamental meridional and the outer two Taylor vortices produces outward bulges in the contours.

$800 > Re > 740$ (the lower Re limit of existence of the 2-vortex flow), the 1-vortex flow is the more efficient of the two flows. The Taylor vortices in figure 13 each have a diameter approximately equal to σ although the pair closer to the equator (and subject to a greater centrifugal force) is larger and has a greater velocity.

The signs of the circulations of the vortices in figure 13 alternate as θ increases from 0 to π. Each vortex is separated from its neighbour by a nearly straight inflow or outflow that extends from the inner to the outer radial boundary. There are no stagnation points that do not lie on one of the radial boundaries. The 2-vortex flow is similar to the 0-vortex flow in that the equator is an outflow boundary. Figure 2 shows that the torque-Reynolds number relationship of the 2-vortex flow is a smooth continuation of the 0-vortex flow. The implications of this fact with respect to transitions between the two flows is discussed in Part 2. The large basic vortices in the 2-vortex flow are pinched at large Re. The flow in figure 13 shows the beginning of a pinch at approximately 3σ from the equator. The contours of constant azimuthal velocity shown in figure 14 bulge outward at the equator in accordance with the fact that the equator is an outflow boundary of the equatorial vortices. The outflow boundary between the Taylor vortex farther from the equator and the large basic vortex is also clearly visible in figure 14 as the outward bulge at a distance of 2σ from the equator.

The energy spectra are shown in figure 15. The spectra of the 2-vortex flow are scalloped and similar to the 1-vortex flow spectra. Notice that figure 15 shows a double scalloping with smaller, thinner scallops interspersed between the larger ones. The two types of scallops are due to the fact that there are two Taylor-vortex pairs near the equator.

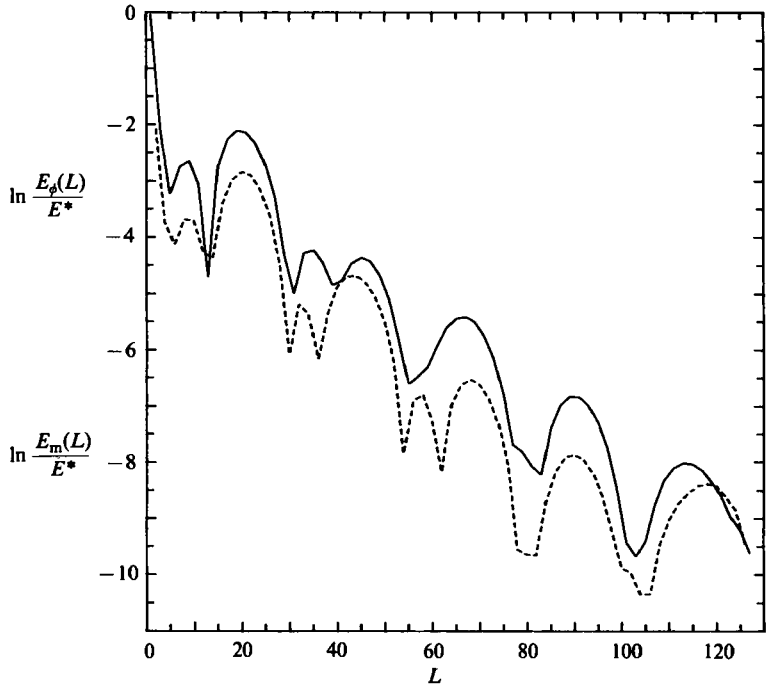

FIGURE 15. $E_\phi(L)$ and $E_m(L)$ (plotted as in figure 6) of the flow in figures 13 and 14. The double scallops – small thin scallops between large wide scallops – are due to the fact that there are two Taylor-vortex pairs close to the equator.

5. Discussion

We have shown that our initial-value code produces solutions that are self-consistent, agree with other numerical calculations, and are supported by laboratory experiments. The most rigorous internal numerical tests that we have performed are those that determine how well the angular momentum and kinetic energy balance equations are satisfied. During the rather complicated transition from 0- to 1-vortex flow (described in Part 2) the angular momentum balance is good to $O(10^{-6})$ and the energy balance to $O(10^{-4})$. Our numerical results are in good agreement with the steady-state solutions found by Schrauf (1983 and private communication) and by Bartels (1982). Considering the fact that the torques are difficult to measure in the laboratory to better than a few per cent, our numerically calculated torques of the 0-, 1- and 2-vortex flows agree quite well with those measured by Wimmer (1976). However, we believe that Wimmer's experimental values of the torque are systematically too large by approximately 7%. In the absence of laser-Doppler velocimetry measurements of the fluid velocity field as a function of position, we believe that the best comparison between numerical and laboratory findings is the measurement of Taylor-vortex size as a function of Reynolds number. Our agreement with Wimmer's high-precision laboratory measurements of Taylor-vortex size are excellent.

The three types of steady-state axisymmetric equilibria that we have found are reflection-symmetric about the equator. At present, we have been unable to find any non-reflection-symmetric steady flows. The 0-, 1- and 2-vortex flows (as well as Taylor–Couette flow in finite cylinders) all show pinches in the large basic vortex at sufficiently large Reynolds number. Pinches are different from Taylor vortices, the

latter being defined by the nearly straight inflow/outflow boundaries along streamlines that extend all the way from the inner to the outer spheres. Both pinches and Taylor vortices mix angular momentum among different radii, thereby decreasing the angular momentum gradient of the flow. The curious thing about pinches is this: In Taylor-vortex flow a fluid particle moves along a streamline near the inner spherical boundary, until it enters the Taylor vortex, where it finds itself thrown centrifugally outward. It is then carried to the outer boundary. In a pinched flow a fluid moves along the inner boundary until it enters the pinch and is thrown radially outward. At the centre of the pinch there is a restoring force, and the fluid particle is carried back to the inner sphere. The restoring force at the centre of the pinch is somewhat puzzling. The force is due to the increased pressure head associated with the stagnation point at the centre of the pinch, but the exact dynamics of how the stagnation point forms, and what prevents the radially outward-moving, centrifugally accelerated fluid in the pinch from breaking through the stagnation point all the way to the outer spherical boundary (and thereby destroying the stagnation point) has not been explained.

The 1- and 2-vortex flows that we have found both have strong radial velocities at the equator, but with opposite signs. The signs at the equator are determined by the fact that (i) meridional vortices alternate in the sign of their circulations (two vortices of the same sign cannot be next to each other) and (ii) the poles are always inflow boundaries. This means that during transitions between a flow with an odd number of Taylor-vortex pairs and a flow with an even number (or vice versa), the radial flow at the equator must change direction. This change of direction is discussed in Part 2.

We thank K. Buhler, G. Schrauf and M. Wimmer for the private communication of their experimental or numerical results. We also thank L. Koschmieder, S. Orszag, and J. Zierep for useful discussions. This work was supported in part by the National Science Foundation grants MEA-82-1569, MEA-84-10412, AST-82-10933 and AST-84-12170. The numerical calculations were carried out on the CRAY-1 computers at the National Center for Atmospheric Research (NCAR) which is operated by the National Science Foundation.

REFERENCES

AMES, W. F. 1977 *Numerical Methods for Partial Differential Equations.* Academic.

ASTAF'EVA, N. M., VVEDENSKAYA, N. D. & YAVORSKAYA, I. M. 1978 Numerical study of nonlinear axisymmetric flow of fluid between two concentric rotating spheres. In *Sixth Intl Conf. on Num. Methods in Fluid Dyn.* Lecture Notes in Physics, vol. 90 (ed. H. Cabannes, M. Holt, & V. Rusanov), pp. 56–63. Springer.

BARTELS, F. 1982 Taylor vortices between two concentric rotating spheres. *J. Fluid Mech.* **119**, 1–25.

BELYAEV, Y. N., MONAKHOV, A. A. & YAVORSKAYA, I. M. 1978 Stability of spherical Couette flow in thick layers when the inner sphere revolves. *Fluid Dyn.* **2**, 162–168. (Transl. *Izv. AN SSSR. Mekh. Zhidkosti i Gaza* **2**, 9–15.)

BENJAMIN, T. B. 1978*a* Bifurcation phenomena in steady flows of a viscous fluid. I: Theory. *Proc. R. Soc. Lond.* A **359**, 1–26.

BENJAMIN, T. B. 1978*b* Bifurcation phenomena in steady flows of a viscous fluid. II: Experiments. *Proc. R. Soc. Lond.* A **359**, 27–43.

BENJAMIN, T. B. & MULLIN, T. 1981 Anomalous modes in the Taylor experiment. *Proc. R. Soc. Lond.* A **377**, 221–249.

BENJAMIN, T. B. & MULLIN, T. 1982 Notes on the multiplicity of flows in the Taylor experiment. *J. Fluid Mech.* **121**, 219–230.

BONNET, J. P. & ALZIARY DE ROQUEFORT, T. 1976 Ecoulement entre deux sphères concentriques en rotation. *J. Méc.* **15**, 373–397.

BRATUKHIN, I. K. 1961 On the evaluation of the critical Reynolds number for the flow between two rotating surfaces. *J. Appl. Maths Mech.* **25**, 1286–1299. (Transl. *Prikl. Mat. i Mekh.* **25**, 858–866.)

CLIFFE, A. 1983 Numerical calculations of two-cell and single-cell Taylor flows. *J. Fluid Mech.* **135**, 219–233.

DAHLQUIST, G., BJORCK, A. & ANDERSON, N. 1974 *Numerical Methods.* Prentice-Hall.

DENNIS, S. C. R. & QUARTAPELLE, L. 1984 Finite difference solution to the flow between two rotating spheres. *Computers and Fluids* **12**, 77–92.

EDMONDS, A. E. 1960 *Angular Momentum in Quantum Mechanics.* Princeton University Press.

GOTTLIEB, D. & ORSZAG, S. A. 1977 *Numerical Analysis of Spectral Methods: Theory and Applications.* Philadelphia: SIAM.

HAIDVOGEL, D. B. & ZANG, T. 1979 Accurate solutions of Poisson's equation by expansion in Chebyshev polynomials. *J. Comp. Phys.* **30**, 167–180.

HOWARTH, L. 1954 Note on the boundary layer on a rotating sphere. *Phil. Mag.* **42**, 1308–1315.

KHLEBUTIN, G. N. 1968 Stability of fluid motion between a rotating and a stationary concentric sphere. *Fluid Dyn.* **3**, 31–32. (Transl. *Izv. AN SSSR. Mekh. Zhidkosti i Gaza* **3**, 53–56.)

LANCZOS, C. 1956 *Applied Analysis.* Prentice-Hall.

MARCUS, P. S. 1984*a* Simulation of Taylor–Couette flow. Part 1. Numerical methods and comparison with experiment. *J. Fluid Mech.* **146**, 45–64.

MARCUS, P. S. 1984*b* Simulation of Taylor–Couette flow. Part 2. Numerical results for wavy-vortex flow with one travelling wave. *J. Fluid Mech.* **146**, 65–113.

MARCUS, P. S. & TUCKERMAN, L. S. 1987 Simulation of flow between concentric rotating spheres. Part 2. Transitions. *J. Fluid Mech.* **185**, 31–66.

MULLIN, T. 1982 Mutations of steady cellular flows in the Taylor experiment. *J. Fluid Mech.* **121**, 207–218.

MUNSON, B. R. & JOSEPH, D. D. 1971*a* Viscous incompressible flow between concentric rotating spheres. Part 1. Basic flow. *J. Fluid Mech.* **49**, 289–303.

MUNSON, B. R. & JOSEPH, D. D. 1971*b* Viscous incompressible flow between concentric rotating spheres. Part 2. Hydrodynamic stability. *J. Fluid Mech.* **49**, 305–318.

MUNSON, B. R. & MENGUTURK, M. 1975 Viscous incompressible flow between concentric rotating spheres. Part 3. Linear stability and experiments. *J. Fluid Mech.* **69**, 705–719.

ROESNER, K. G. 1977 Numerical calculation of hydrodynamic stability problems with time-dependent boundary conditions. In *Sixth Intl Conf. on Num. Methods in Fluid Dyn.* (ed, H. Cabannes, M. Holt & V. Rusanav), Lecture Notes in Physics, vol. 90, pp. 1–25. Springer.

SAWATZKI, O. & ZIEREP, J. 1970 Das Stromfeld im Spalt zwischen zwei konzentrischen Kugelflächen, von denen die innere rotiert. *Acta Mechanica* **9**, 13–35.

SCHRAUF, G. 1983 Lösungen der Navier–Stokes Gleichungen für stationäre Strömungen im Kugelspalt. Ph.D. thesis, Universität Bonn.

SOWARD, A. M. & JONES, C. A. 1983 The linear stability of the flow in the narrow gap between two concentric rotating spheres. *Q. J. Mech. Appl. Maths* **36**, 19–42.

TUCKERMAN, L. S. 1983 Formation of Taylor vortices in spherical Couette flow. PhD thesis, Massachusetts Institute of Technology.

WALTON, I. C. 1978 The linear stability of the flow in a narrow spherical annulus. *J. Fluid Mech.* **86**, 673–693.

WIMMER, M. 1976 Experiments on a viscous fluid flow between concentric rotating spheres. *J. Fluid Mech.* **78**, 317–335.

YAKUSHIN, V. L. 1969 Instability of fluid motion in thin spherical layer. *Fluid Dyn.* **4**, 83–84. (Transl. *Izv. AN SSSR. Mekh. Zhidkosti i Gaza* **4**, 119–123.)

YAVORSKAYA, I. M., BELYAEV, Y. N. & MONAKHOV, A. A. 1977 Stability investigation and secondary flows in rotating spherical layers at arbitrary Rossby numbers. *Sov. Phys. Dokl.* **22**, 717–719. (Transl. *Dokl. Akad. Nauk SSSR* **237**, 804–807.)

ZIEREP, J. & SAWATZKI, O. 1970 Three dimensional instabilities and vortices between two rotating spheres. In *8th Symp. Naval Hydrodyn.* pp. 275–288.